Dwi Astuti Cahyasiwi - Integrated and Independent Solid Microwave Sensor with Dual-Band Bandpass Filter Through Unified Mux-Demux Structure

by Layanan Perpustakaan UHAMKA

This article has been accepted for publication in IEEE Sensors Journal. This is the author's version which has not been fully edited and
content may change prior to final publication. Citation information: DOI 10.1109/JSEN.2024.3397310

Integrated and Independent Solid Microwave Sensor with Dual-Band Bandpass Filter Through Unified Mux-Demux Structure

Teguh Firmansyah, *Member, IEEE*, Supriyanto Praptodiyono, Imamul Muttakin, Muh. Wildan, Dwi Astuti Cahyasiwi, Yusnita Rahayu, Hepi Ludiyati, Ken Paramayudha, Yuyu Wahyu, Syah Alam, Mudrik Alaydrus, *Senior Member, IEEE*, and Jun Kondoh, *Member, IEEE*

***Abstract*—Multifunctional, integrated, and independent microwave sensor (MS) with dual-band bandpass filter (BPF) for solid material characterization and radio frequency communication is presented. The proposed device is developed using a multi-coupled line resonator structure to integrate both multiplexing (MUX) and demultiplexing functionalities (DEMUX). On the input side, the circuit behaves like a MUX, divided into three main sections: Path I, Path II, and the MS structure. Path I and Path II sections feature a pair of coupled-line configurations for the lower-band BPF (LB-BPF) with ladder-based resonators and upper-band BPF (UB-BPF) with hairpin-based resonators, respectively. Additionally, the MS structure employs a ring resonator configuration, positioned between Path I and Path II. On the output side, the circuit behaves like a DEMUX, combining back into a single port. As a result, the dual-band BPF has frequency centers of 1.80 GHz (LB-BPF) and 2.56 GHz (UB-BPF) suitable for 4G and 5G applications, respectively. Moreover, the dual-band BPF exhibits independent characteristics, with easily controllable frequency centers and fractional bandwidths. Furthermore, for the MS function, the frequency of maximum transmission (MT) and the transmission zero (TZ) were utilized for MS evaluation. Solid materials with low permittivity (ε_r) ranging from 1 to 9.5 were used as samples. The MS achieved a normalized sensitivity of 2.60% and 1.98% for MT and TZ, respectively. Interestingly, the integration of LB-BPF, UB-BPF, and MS shows independent performances and does not influence each other. This behavior is linked to distinctive electric field locations. Finally, compared to prior structures, the proposed design offers several advantages, including: 1) multifunctional capability by combining a dual-band MS and dual-band BPF, 2) independent and simultaneous characteristics, and 3) full integration with a simple structure based on 2-port single-layered substrate design.**

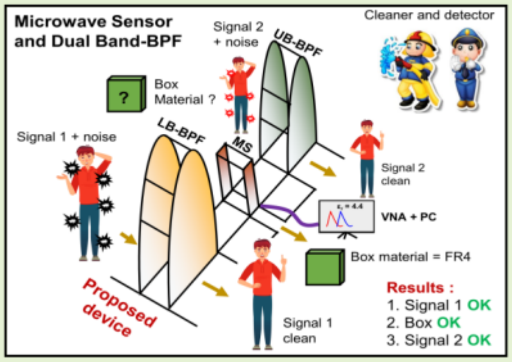

***Index Terms*—**Dual-band BPF, integrated microwave sensor, multifunctional, MUX-DEMUX, and ring resonator.

I. Introduction

MICROWAVE sensors (MS) have been the subject of intensive study and development in both academic and industrial circles, owing to their numerous advantages such as high sensitivity, high selectivity, and ease of fabrication. These sensors operate based on radio frequency (RF) signals by detecting changes in the environment and subsequently shifting the frequency, phase, amplitude, or reflection values. The MS has a wide range of applications, such as physical sensors, chemical sensors, and biosensors. In addition, the MS can also detect solid, liquid, and gas phases. The key principle behind MS is the exploitation of permittivity or permeability of the environment especially for solid material [1]–[3]. However, it poses limitations particularly in the context of future communication devices where the multifunctionality between sensor and communication is needed. The multifunctional integration of sensor and communication, particularly dual-band bandpass filters, is important for establishing an efficient and low noise system.

Several interesting dual-band BPFs were proposed: A. Ghaderi et al. [4] introduced a compact dual-band BPF using T-shaped resonators, while F. Wei et al. [5] presented a compact dual-band BPF with a wide stopband. Additionally, a dual-band BPF with reconfigurable capability was proposed by [6]. These dual-band BPFs exhibit good performance, leveraging impedance analysis. However, the proposed dual-band BPFs are limited to monofunctional capability as BPFs only. Furthermore, there is a need for the combination of BPFs and

---

This work was supported in part by the Ministry of Research, Technology and Higher Education Indonesia. Grant LPPM UNTIRTA 2024.

Teguh Firmansyah, Supriyanto Praptodiyono, and Imamul Muttakin are with Department of Electrical Engineering, Universitas Sultan Ageng Tirtayasa, Cilegon, Banten, 42435, Indonesia. (corresponding author: teguhfirmansyah@untirta.ac.id).

Please see the Acknowledgment section of this article for the author affiliations.

This article has been accepted for publication in IEEE Sensors Journal. This is the author's version which has not been fully edited and content may change prior to final publication. Citation information: DOI 10.1109/JSEN.2024.3397310

MS, especially in the Internet of Things (IoT) and 4G/5G era. Sensors collect real-time data from the environment, while communications facilitate fast, long-distance data transfer. This can enhance energy efficiency and bolster support for the IoT. Overall, a swift response to environmental changes combined with communication can significantly amplify productivity and efficiency, such as reducing the number of ports, having a smaller size structure, and achieving more efficient power due to simultaneous functionality.

To overcome monofunctional capability limitation, several multifunctional devices and/or sensors with multiple tasks simultaneously were proposed [7]–[21]. In detail, these sensors integrate additional functionalities, such as antenna, oscillator [19], balance/unbalance [11], duplexer [16], and BPF capabilities, alongside their sensing capabilities. By combining these functionalities into an integrated device/sensor, the overall efficiency and versatility of the devices can be greatly enhanced. In detail, there have been notable advancements in integrating antennas with microwave sensors, as documented in [12], [13], [18], [21]. These studies have introduced various strategies to enhance the performance of these integrated systems. One key approach involves impedance matching of an antenna as a sensor, as highlighted in [13]. This technique results in a shift in the resonance frequency of the antenna [15]. Another significant development is the proposal of an active integrated antenna for permittivity sensing, as presented in [8]. In this case, interdigital structures are employed as part of the oscillator element. Consequently, when the sample is loaded, the resonance frequency of the antenna changes accordingly.

Several studies that combine BPF and MS are proposed by [10], [14], [20], [22]. In detail, the MS has a function for displacement application. In detail, ref [10] is focused on the bandstop filter structure. Then, the movable layer can be used for displacement sensing based on the phase of the reflection coefficient. Moreover, the displacement sensing strategy has been extended in works like [14], [20], [22] to incorporate noncontact characteristics, which function to reduce friction and extend the range of displacement measurement. However, the primary limitation of the sensors discussed in [10], [14], [20], [22] is the presence of ambiguities and a lack of independent characteristics, which can make interpretation challenging.

In general, multifunctional MS/device structures face several major challenges: 1) The exhibition of a high degree of complexity, requiring additional insulator structures between the device and the MS. This complexity can complicate the manufacturing process and increase the chances of operational issues. 2) The requirement of an additional power supply to support the various functionalities. This dependence on external power sources can be inconvenient and limit portability. 3) The limitation on supporting typically only a single-band communication system with a fixed band. This condition restricts their versatility and compatibility. 4) Many proposed multifunctional devices often offer switchable functionalities, meaning that only one feature can be active at a given time. This constraint prevents the simultaneous operation of multiple functions, potentially reducing efficiency and causing inconvenience. 5) In some cases, the different functions integrated within a combined device may not operate independently. The performance of one function may be affected by the operation of another, leading to compromised performance and unpredictable behavior. 6) The ambiguous and non-independent characteristics of multifunctional devices. These devices often introduce uncertainties regarding their performance and limitations. It can be challenging to precisely define their capabilities and ensure consistent performance across all functionalities. Consequently, the challenges in developing more agile and versatile multifunctional MS/devices are numerous, leaving many voids and open problems to address.

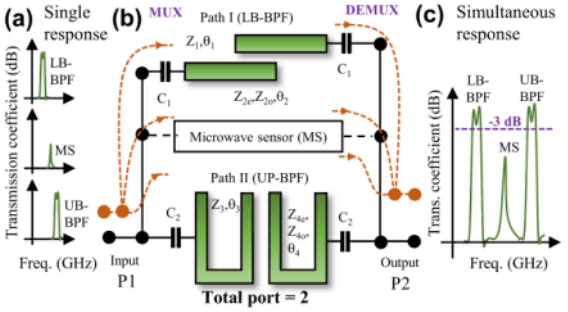

Fig. 1. A proposed of multifunctional and independent dual-band bandpass filter with a solid microwave sensor. (a) The transmission coefficient response of each branch. (b) The proposed technique for branch integration. The circuit functions as a mux on the input side and as a demux on the output side. Path I and path II serve as lower-band bandpass filters (LB-BPF) and upper-band (UB-BPF) filters, respectively. Additionally, capacitance C_1 and C_2 represent the coupling characteristics between the input/output feed and path I and path II, respectively. A microwave sensor (MS) is positioned in the middle between Path I and Path II. (c) Simultaneous response of the transmission coefficient of the proposed device.

As a novelty, the proposed structure offers several novel features and advantages, as outlined below.

1) A multifunctional, integrated, and independent MS and dual-band BPF for solid material characterization and radio frequency communication is presented. The proposed device is designed using multi-coupled line resonators that unify the multiplexer-demultiplexer (MUX-DEMUX) structure. On the input side, the circuit functions as a MUX, and on the output side, it operates as a DEMUX, recombining into a single port, as shown in **Fig. 1(a)-(b).**
2) The integration of the BPF and MS components ensures independent operation without mutual interference. This independent behavior is a result of the distinct electric field (**E**) locations. Importantly, the transmission coefficient ($|S_{21}|$) of the BPFs and MS are distinctive, with BPFs demonstrating higher and wider S_{21} responses compared to the MS, as shown in **Fig. 1(c).** These distinctions significantly reduce interpretation ambiguity.
3) The dual-band BPFs provide easily controllable and independent characteristics in terms of frequency center (f_c) and fractional bandwidth (FBW).
4) For the MS function, we utilize the frequencies at the maximum transmission (MT) and transmission zero (TZ)

This article has been accepted for publication in IEEE Sensors Journal. This is the author's version which has not been fully edited and content may change prior to final publication. Citation information: DOI 10.1109/JSEN.2024.3397310

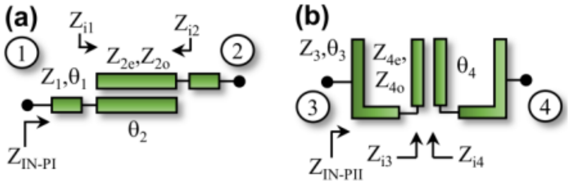

Fig. 2. A detailed multi-coupled line (CL) structure. (a) The Z_1 is the impedance between the feed line and CL. Moreover, The Z_{2e} and Z_{2o} are the even- and odd-mode impedance of path I. (b) The Z_3 is the impedance between the feed line and CL. Then, the Z_{4e} and Z_{4o} are the even- and odd-mode impedance of Path II.

for sensing evaluation. This approach provides a greater degree of freedom, especially for material characterization, and facilitates more robust analysis.

5) Compared to standalone BPF and MS devices, the proposed structure reduces the number of ports by 66% (from 6 ports to 2 ports). Additionally, the device features a simple single-layered substrate design, ensuring ease of implementation.

The work is organized as follows. In Section II, we discuss the proposed independent dual-band BPF based on the multi-coupled line structure. This section includes a study of the impedance characteristics of each resonator. We then explain the dual-band filter circuit, covering the response of each branch and the combination of the two branches. This section also provides a discussion of the independent characteristics of the two filters, highlighting that adjustments to the center frequency and bandwidth are trivial. In Section III, the discussion focuses on the introduction of a ring resonator into the middle of Path I and Path II, along with the optimization of their dimensions and equivalent circuits. Following this, the section discusses microwave sensors, focusing on the placement of materials and the analysis of electric field distribution. It then proceeds to simulate transmission efficiency values with changes in various material permittivity and simulations involving changes in the loss tangent. Section IV is dedicated to fabrication and sensor measurements using various solid materials. This section also includes measurements of frequency shifts and sensitivity values. Finally, the conclusions are presented in Section V.

II. DUAL BAND BPF BASED ON MULTI-COUPLED LINE THROUGH UNIFIED MUX-DEMUX STRUCTURE

Fig. 1(a) illustrates the structure of each branch of the MUX. The upper structure represents Path I, referred to as the LB-BPF structure, which resembles the shape of a BPF ladder. Meanwhile, at the bottom is the Path II structure, which serves as UB-BPF and exhibits a BPF hairpin shape. An MS structure is positioned between Path I and Path II with a ring-resonator shape functioning as the probe. We can observe that if the proposed device operates in a monofunctional mode, it will require 6 connectors. This could be considered a waste of resources. **Fig. 1(a)** illustrates the response plan for each MUX branch. Here, we designed and planned the $|S_{21}|$ response of the BPF to have a wider bandwidth and a higher magnitude value. In contrast, the response of the MS is more sharply defined, with a lower magnitude. This characteristic plays a crucial role in eliminating ambiguity between the functions of BPF and MS.

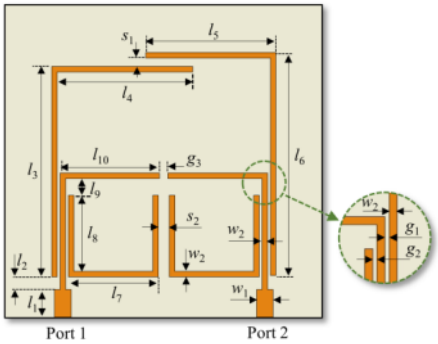

Fig. 3. A complete layout of Path I and Path II for dual-band BPF application. Here, w_1 = 3.0 mm, w_2 = 1.0 mm, l_1 = 5.0 mm, l_2 = 3.0 mm, l_3 = 37.0 mm, l_4 = 25.5 mm, l_5 = 23.5 mm, l_6 = 39.0 mm, l_7 = 16 mm, l_8 = 14.75 mm, l_9 = 3.0 mm, l_{10} = 18.0 mm, g_1 = 0.5 mm, g_2 = 0.5 mm, and g_3 = 0.5 mm.

Fig. 1(b) illustrates the proposed integration of MUX and DEMUX using the multi-coupled line method. Specifically, the structure functions as a MUX on the input side, dividing one input into three branches. This system is referred to as a MUX because each branch operates at a different frequency. The use of different working frequencies in each branch facilitates the independent evaluation of BPF and MS performance. On the output side, the system recombines into a single branch, resembling a DEMUX system. Consequently, only two connectors are required in total. Therefore, the proposed system has the potential to save 66% of connectors. Meanwhile, **Fig. 1(c)** displays the plan of $|S_{21}|$ response of the dual ports of the proposed structure. There is a significant disparity between the BPF response and the MS response. The MS exhibits a sharper $|S_{21}|$ response with a smaller magnitude.

Fig. 2(a) shows the detailed structure of the LB-BPF circuit. Additionally, Z_{2e} and Z_{2o} correspond to the even- and odd-mode impedance of Path I. Then, the Z_{i1} is determined by [23], [24]:

$$Z_{i1} = \frac{\{(Z_{2e}-Z_{2o})^2-(Z_{2e}+Z_{2o})^2\cos^2\theta_2\}^{\frac{1}{2}}}{2\sin\theta_2} \tag{1}$$

The relation between the complex propagation with the even- and odd-mode impedances of Path I and the electric length of θ_2 is calculated using the following equation:

$$\cosh(\alpha + j\beta) = \left(\frac{r_1+1}{r_1-1}\right)\cos\theta_2 \tag{2}$$

where $r_1 = Z_{2e}/Z_{2o}$.

Then, **Fig. 2(b)** shows the detailed structure of the UB-BPF circuit. Z_3 represents the impedance between the feed-line and CL. Moreover, Z_{4e} and Z_{4o} are the even- and odd-mode impedance parameters of Path II with electric length of θ_4. The Z_{i3} is determined by [23], [24]:

$$Z_{i3} = -j\sqrt{Z_{4e}Z_{4o}}\cot\theta_4 \tag{3}$$

Then, the relation between the complex propagation with the even- and odd-mode impedances of Path II is determined by:

$$\cosh\alpha = \frac{Z_{4e}+Z_{4o}}{Z_{4e}-Z_{4o}} \tag{4}$$

After calculating all the impedances, the realistic value of

This article has been accepted for publication in IEEE Sensors Journal. This is the author's version which has not been fully edited and
content may change prior to final publication. Citation information: DOI 10.1109/JSEN.2024.3397310

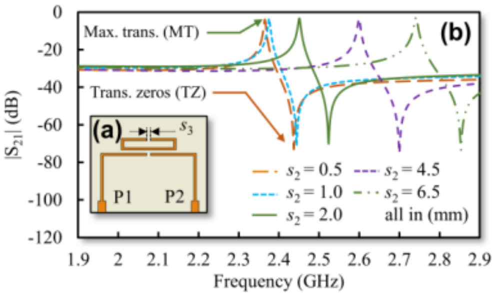

Fig. 4. (a) Transmission coefficient ($|S_{21}|$) values of ring resonator structure with direct source/load coupled line for different values of gap (s_3). The structure will be utilized as an MS. (b) It has the value of maximum transmission coefficient (M_T) and transmission zeros (T_Z).

impedance should be chosen to ensure successful fabrication. Here, the termination port of Z_0 is set as 50 Ω. Moreover, the impedance of Z_1 and Z_3 are 113.0 Ω and 113.0 Ω, respectively. Then, the electric lengths of θ_1, θ_2, θ_3, and θ_4 are 132.2°, 24.1°, 64.1°, and 40.7°, respectively. Furthermore, the even- and odd-mode impedance of Path I and Path II have values of $Z_{2e} = 133.0$ Ω, $Z_{2o} = 94.0$ Ω, and $Z_{4e} = 143.6$ Ω, $Z_{4o} = 92.1$ Ω, respectively.

A. An Independent of Dual-Band BPF Response

Fig. 3 displays detailed circuit dimensions for Path I and Path II. The termination ports are located at the bottom on both the input and output sides. Additionally, on the input side, the supply circuit is directly coupled to LB-BPF and UB-BPF. This coupling strategy serves several purposes, including the distribution of power to various locations, thereby reducing mutual coupling between the two filters (LB-BPF and UB-BPF). A low level of mutual coupling between the passbands ensures that the dual-band BPF responses remain independent of each other. Furthermore, another reason for this configuration is to maintain a high-power level, resulting in a larger $|S_{21}|$ value, which is essential for achieving the desired BPF response.

Moreover, the feeding circuit between the input and output features an extended structure, allowing a low coupling connection between them. This arrangement is commonly referred to as source-load coupling. Utilizing source-load coupling is beneficial for confining and localizing the LB-BPF and UB-BPF locations. Next, a ladder-based structure is employed in the LB-BPF, specifically designed so that the vacant location can be later used for an MS. Furthermore, increasing the distance between the coupling and the MS promotes independent response. Meanwhile, the UB-BPF employs a hairpin-based structure with adjacent capacitive coupling. This design effectively reduces coupling on the feed line located on the top side, which will be used for the MS in the next stages.

In the Supplementary Material, **Fig. S1** at presents a comparison of $|S_{21}|$ and $|S_{11}|$ values for the proposed configuration with Path I only and Path I with Path II. It is evident that Path I generates the LB-BPF. Subsequently, when combined with Path II, a dual-band BPF is achieved. It can be said that Path II generates the UB-BPF. As mentioned at the beginning, the proposed dual-band BPF structure exhibits independent performance. **Fig. S2 (a-d)** illustrates the performance of $|S_{21}|$, displaying an independent response when tuning the center frequency (f_C) and bandwidth (BW).

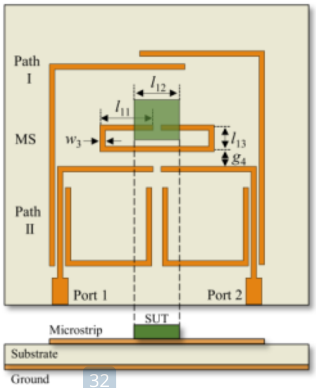

Fig. 5. The final layout of the proposed dual-band filtering sensor based on multi-coupled lines with the ring resonator. The dual-band BPFs were developed using a combination of Path I and Path II structure. Then, the microwave sensor (MS) based on the ring resonator was fabricated in the middle part. Moreover, the illustration also shows the position of the sample under test (SUT).

Specifically, **Fig. S2(a)** demonstrates that the center frequency in LB-BPF (f_{C1}) can be independently adjusted by altering the length of l_A, where $l_A = l_3 + l_4 = l_5 + l_6$. Then, **Fig. S2(b)** illustrates that the bandwidth of the LB-BPF (BW_1) can be independently tuned by modifying the gap of s_1. In addition, **Fig. S2(c)** shows that the frequency center of the UB-BPF (f_{C2}) can be shifted independently by altering the length of l_B, where $l_B = l_7 + 2l_8$. Moreover, **Fig. S2(d)** demonstrates that the bandwidth of the upper-band UB-BPF (BW_2) can be independently tuned by changing the gap s_2. In detail, the f_{C1}/f_{C2} can be adjusted to lower frequencies by increasing the value of l_A/l_B, respectively or by changing the length of the resonator. Then, the BW_1/BW_2 can be reduced by increasing the values of s_1/s_2, respectively, or by changing the coupling distance. In short, the proposed dual-band BPF has frequency centers of 1.8 GHz (LB-BPF) and 2.6 GHz (UB-BPF), suitable for 4G and 5G applications, respectively. The dual-band BPF exhibits independent characteristics, with easily controllable frequency centers and fractional bandwidths.

III. INTEGRATED DUAL-BAND BPF AND SOLID MS BASED ON MULTI-COUPLED LINE STRUCTURE

After optimizing the independent dual-band BPF design, the next stage is to design and optimize the structure of the MS. **Fig. 4(a)** illustrates the proposed structure of the MS. The feeding structure employed in this study is a source-load coupling structure between port 1 and port 2. A ring resonator structure is utilized, which is magnetically coupled to the feeder. Ring resonators offer the advantage of being able to separate the maximum values of the electric field (**E**) and the magnetic field (**H**). The gap position of the ring resonator is positioned away from the source-load coupling position. This is essential to minimize the interaction between the MS and the BPF. Furthermore, there are several key considerations when designing the MS:

1) The MS location must be sufficiently distant from the dual-band BPF to ensure independent performance. This

This article has been accepted for publication in IEEE Sensors Journal. This is the author's version which has not been fully edited and
content may change prior to final publication. Citation information: DOI 10.1109/JSEN.2024.3397310

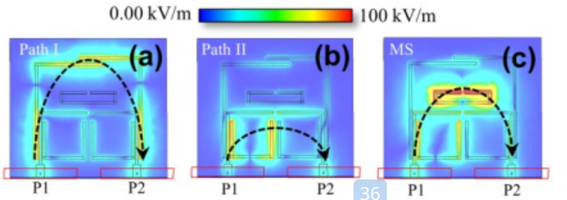

Fig. 6. The electric field distribution (**E**) for (a) Path I, (b) Path II, and (c) MS location. The maximum value of the E field has a different region for each structure. Then, for easy analysis, the E fields have the same scale with a maximum value of 100 kV/m.

can be achieved in two ways: physical separation, as observed between the MS and LB-BPF, or by implementing a source-load blocking structure, as demonstrated in the case of the MS and UB-BPF.

2) To mitigate interference between LB-BPF and UB-BPF, this study suggests placing the working frequency of the MS between the working frequencies of LB-BPF and UB-BPF.
3) It is important to maintain a low S_{21} value for the MS to prevent it from functioning as a BPF.
4) Since the MS will be loaded with samples, the resonant frequency of the MS without samples should be close to the center frequency of the UB-BPF.

To adjust the frequency of the MS, the values of the resonator length and gap can be utilized. **Fig. 4(b)** illustrates the iteration of the gap value (s_3) and its correlation with the locations of the maximum transmission coefficient (MT) frequency and transmission zeros (TZ) frequency. In this study, two sensor locations were employed, namely, TZ-based and MT-based frequencies.

Fig. S3(a) depicts an equivalent circuit model of a ring resonator with magnetic coupling to the feedline. The input and output terminations are set to 50 Ω. Additionally, the source-load coupling is represented by a value of $C_{SL} = 0.1$ pF. On the ring resonator (RR) side, the resonator values are represented as $L_{RS} = 12.9$ nH, $C_{RS} = 0.5$ pF, and $R_{RS} = 1.0$ Ω. Meanwhile, the gap value in the RR is denoted by the liquid value of $C_{air} = 0.81$ pF. **Fig. S3(b)** presents a comparison of the computational results between the finite element model (FEM) and the equivalent circuit model (ECM) of the RR. The results indicate that both the FEM and ECM yield similar values and share the same resonance frequency values, as well as identical MT and TZ values.

Then, the introduction of a sample to the MS leads to a change in the capacitance value within the gap, resulting in alterations to the C_{air} value. These changes lead to shifts in the MT and TZ values. **Fig. 5** displays the final layout of the proposed integrated dual-band BPF and MS, based on multi-coupled lines with a ring resonator, through a unified MUX-DEMUX structure. The dual-band BPFs were developed using a combination of Path I and Path II structures. Subsequently, the MS, based on the ring resonator, was fabricated in the middle portion. Furthermore, the illustration also indicates the position of the sample under test (SUT). Additionally, a perpendicular view is provided to enhance clarity in visualization. **Fig. 6(a), 6(b), and 6(c)** depict the electric field distribution at resonance conditions for Path I, Path II, and MS, respectively. It can be clearly seen that the different functions have different directions.

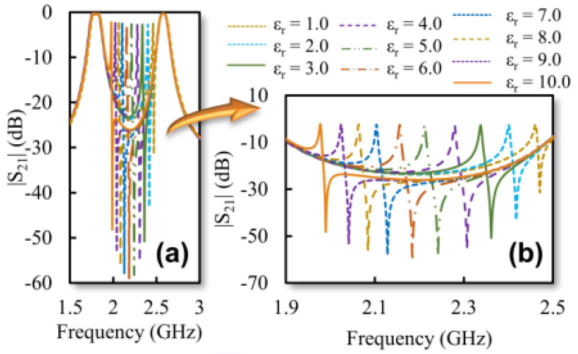

Fig. 7. (a) Simulation results of transmission coefficient parameter ($|S_{21}|$) with the broadband response of the proposed dual-band filtering sensor for different values of relative permittivity (ε_r) from 1.0 to 10.0 of the sample under test (SUT). (b) Simulation result of transmission coefficient parameter ($|S_{21}|$) with detail around the maximum transmission (MT) and transmission zeros (TZ) value.

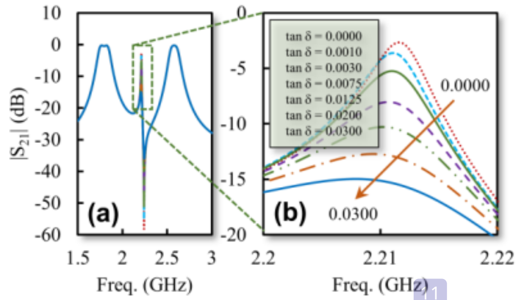

Fig. 8. (a) Simulation results of $|S_{21}|$ with broadband response of the proposed dual band filtering-sensor for different value of dielectric loss (tan δ) of the sample from 0.0 to 0.03 with relative permittivity of SUT of 5.00. (b) detail value of $|S_{21}|$ around in-band MT.

Each structure has different regions with maximum E-field. For ease of analysis, the E-fields are normalized to a maximum value of 100 kV/m. When the simulation is run at f_{C1}, the maximum E-field value is observed on Path I. Conversely, when the simulation is conducted at f_{C2}, the E-field value is observed on Path II. Finally, when the simulation is performed at the MS frequency, the E-field value is found in the MS structure. This simulation demonstrates that each sub-device, such as LB-BPF, UB-BPF, and MS, operates independently and does not influence the others.

Fig. 7(a) depicts simulation results of $|S_{21}|$ with broadband response from 1.5 GHz to 3 GHz for the proposed dual-band BPF and MS at different values of relative permittivity (ε_r) for the sample under test (SUT), which ranges from 1.0 to 10.0. The SUT size used is 10 mm x 10 mm x 1.5 mm with a constant dielectric loss (tan δ). The simulated sample with $\varepsilon_r = 1.0$ indicates that the device has not been loaded with a sample and remains in free-air condition. Meanwhile, the simulation results with the sample show that when $\varepsilon_r = 2.0$, the frequency shift is significant. However, a significantly larger shift in the value of $|S_{21}|$ occurs when $\varepsilon_r = 10.0$. In general, adding samples does not affect the performance of the dual-band BPF, and the two bands of BPF exhibit independent performance. **Fig. 7(b)** depicts a

This article has been accepted for publication in IEEE Sensors Journal. This is the author's version which has not been fully edited and content may change prior to final publication. Citation information: DOI 10.1109/JSEN.2024.3397310

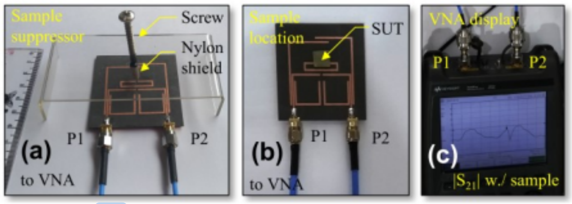

Fig. 9. (a) A photograph of the dual-band filtering sensor and the measurement setup for evaluation of different SUTs. The holder, screw, and nylon shield were utilized for the SUT suppressor. (b) A photograph of the sample location of SUT. (c) The VNA display of $|S_{21}|$ measurement result with SUT was loaded to the dual-band filtering sensor.

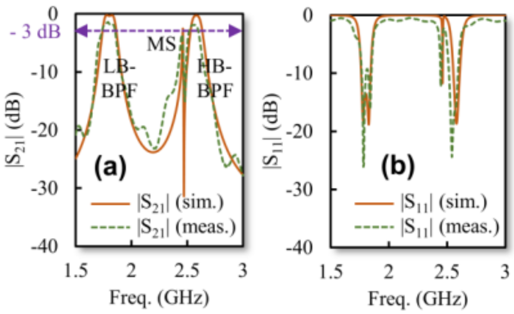

Fig. 10. Comparison between simulation and measurement of (a) magnitude $|S_{21}|$ and the detail value of magnitude $|S_{21}|$ around the 0 dB to measure and calculate the bandwidth (BW), and (b) magnitude $|S_{11}|$ of integrated dual-band BPF and MS.

simulation result of $|S_{21}|$ with details regarding the values of MT and TZ. To enhance detection clarity, we propose using the frequencies of MT and TZ as sensor indicators in simulation. Consequently, the sensor gains a higher degree of freedom to operate.

Fig. 8(a) shows the simulation result of $|S_{21}|$ with a broadband response for the proposed dual-band filtering sensor at different values of dielectric loss ($\tan\delta$) of the sample, ranging from 0.0 to 0.03, with relative permittivity (ε_r) of SUT at 5.00. Then, **Fig 8(b)** illustrates detailed $|S_{21}|$ values around the in-band MT. Higher dielectric loss generates a lower value of $|S_{21}|$. This simulation is important to show that the proposed sensor can also function as a dielectric loss sensor. Similar to different permittivity loads, variation in dielectric loss ($\tan\delta$) does not impact the BPF response.

IV. FABRICATION, MEASUREMENTS, CROSS-SECTIONAL EFFECT, AND SENSOR EVALUATION OF INTEGRATED DUAL-BAND BPF AND MS

A. Fabrication and Measurement Setup

To verify the proposed concept, the dual-band BPF and MS device were fabricated on a Rogers RT/Duroid 5880 substrate with ε_r = 2.2, and a loss tangent ($\tan\delta$) of 0.0009, and a thickness of 1.55 mm. A photograph of the dual-band BPF-MS and the measurement setup for evaluating various SUTs is shown in **Fig. 9(a).** Here, the holder, screws, and nylon shield were used as SUT suppressors. It should be noted that SUT suppressors are essential for establishing direct contact between the SUT and the device.

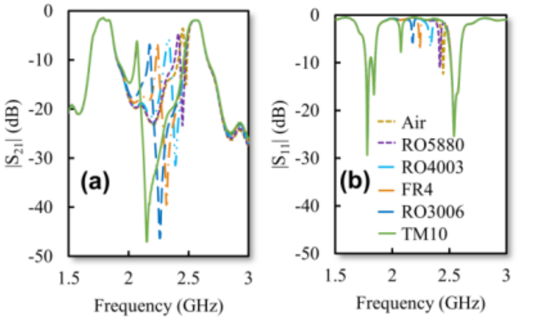

Fig. 11. (a) Measurement results of $|S_{21}|$ with the broadband response of the dual-band filtering sensor for different SUT. (b) Measurement result of $|S_{11}|$ with the broadband response of the dual-band filtering-sensor for different SUT

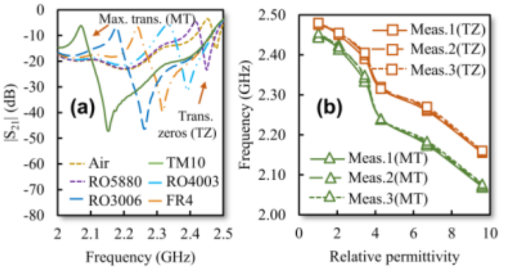

Fig. 12. (a) Measurement results of transmission coefficient parameter ($|S_{21}|$) with detail around the maximum transmission (MT) and transmission zeros (TZ) value. (b) Measurement result of the frequency value at the maximum transmission (MT) and transmission zeros (TZ) with three times repeatability.

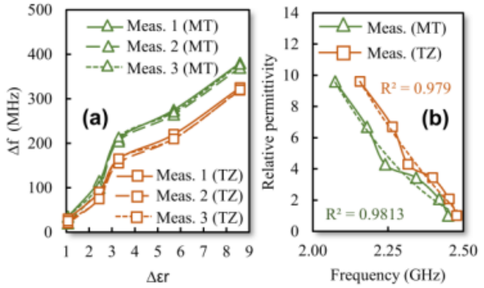

Fig. 13. (a) Measurement results of the Δf and $\Delta\varepsilon_r$ compared to unloaded condition (such as f_{air} and ε_r = 1.00) with three times repeatability. (b) Relation between the frequency value at the maximum transmission (MT) and transmission zeros (TZ) with ε_r value for regression purposes.

They can also reduce the air gap and minimize measurement mismatches. To ensure more stable data, this measurement strategy was implemented for all samples. Several points to note include that the nylon shield has low permittivity, and the pressure was not applied at the maximum E field. **Fig. 9(b)** depicts a photograph of the sample location of the SUT in the proposed device. The device is connected to a vector network analyzer (VNA) through port 1 (50 Ω) and port 2 (50 Ω). Furthermore, **Fig. 9(c)** shows the VNA display of the $|S_{21}|$ measurement result with the SUT loaded into the dual-band BPF-MS device. It can be observed that the $|S_{21}|$ has three peaks. The wide peaks function as the LB-BPF and UB-BPF, while the sharp peak and sharp valley serve as the MS at MT

This article has been accepted for publication in IEEE Sensors Journal. This is the author's version which has not been fully edited and content may change prior to final publication. Citation information: DOI 10.1109/JSEN.2024.3397310

TABLE I.
COMPARISON WITH STATE-OF-THE-ART INTEGRATED MS AND OTHER DEVICES

Ref.	Type	Range of ε_r	Num. of freq.	f_n (GHz)	Size ($\lambda_g \times \lambda_g$)	Integrated application	FBW (%)	FDR $\Delta f/\Delta\varepsilon_r$	NS. (%)	Parameter and integrated features							
										Tunable		Not req. insulator	Not req. power supply	Not ambiguous result	Inde-pendent	Co-work Dualband	Functionalities
										f_c	BW						
Microwave sensors and other devices such as antenna																	
[17]	RFID Antenna	1.00 - 12.85	1	2.45	0.62× 0.40	MS/ Antenna	2.04	2.60	0.10	-	-	-	-	-	-	-	switchable
[31]	Active tag antenna	1.00 - 10.20	1	7.00	0.56× 0.84	MS/ Antenna	100.0	23.90	0.34	-	-	-	no	-	-	-	switchable
[32]	Planar EC resonator	1.00 - 10.20	1	2.41	0.28× 0.24	MS	20.40	90.00	3.73	-	-	-	-	-	-	-	alternately
						MS											
[33]	Dual U-shaped	1.00 - 4.30	2	1.21	0.20× 0.20	MS	0.96	9.09	0.76	yes	-	-	-	-	-	-	alternately
				2.10		MS	0.53	24.24	1.15	yes	-						
[21]	Frequency SMF	2.30- 26.00	2	2.45	0.54× 0.21	Antenna	16.73	-	-	yes	-	no	-	-	yes	-	simultaneous
				4.75		MS	-	NA	NA	-	-						
[18]	Multilayer cavity	1.00 - 10.20	2	9.67	1.93× 1.29	Antenna	2.80	-	-	yes	-	-	-	-	yes	-	simultaneous
				12.30		MS	-	78.00	0.64	-	-						
Microwave sensors and bandpass filter																	
[10]	TL-SSRs	Displacement sensor	1	1.80	0.34× 0.11	Bandstop/ MS	5.3	20 MHz /o	NA	yes	-	-	-	no	-	-	alternately
[14]	TFS-coupled	Displacement sensor	1	1.80	0.14× 0.18	UWB-BPF /MS	110.0	227 MHz /o	NA	yes	-	-	-	no	-	-	alternately
[22]	ML: TSI	Displacement sensor	1	0.96	0.20× 0.29	Bandpass/ MS	110.0	0.20 MHz /o	NA	yes	-	-	-	no	-	-	alternately
This work	Unified Mux-Demux	Permittivity sensor 1.00 - 9.50	4	1.80	0.36× 0.33	BPF	3.39	-	-	yes	yes	yes	yes	yes	yes	yes	simultaneous
				2.45		MS	-	63.70	2.60	-	-						
				2.48		MS	-	49.11	1.98	-	-						
				2.56		BPF	3.32	-	-	yes	yes						

*NA = not available information.

and TZ.

Then, **Fig. 10(a)** and **Fig. 10(b)** display a comparison between simulation and measurement results for an integrated dual-band BPF and MS of magnitude $|S_{21}|$ and $|S_{11}|$, respectively. The simulation and measurement data align well. Specifically, the measurement peaks for $|S_{21}|$ are -1.54 dB and -1.91 dB at frequencies of 1.80 GHz and 2.56 GHz, values suitable for low-band BPF (LB-BPF, 4G) and upper-band BPF (UB-BPF, 5G) applications. Additionally, there is a middle peak at -3.59 dB at 2.45 GHz, intended for MS applications. Furthermore, the magnitudes of $|S_{11}|$ are -26.02 dB, -12.3 dB, and -24.38 dB at frequencies of 1.80 GHz, 2.45 GHz, and 2.56 GHz, respectively. These values indicate that the measurement results exhibit good performance for both $|S_{21}|$ and $|S_{11}|$. Moreover, it provides detailed information about the magnitude of $|S_{21}|$ in the vicinity of -3 dB, enabling the measurement and calculation of fractional bandwidth (FBW). This structure demonstrates fractional bandwidths of 3.39% and 3.32% for LB-BPF and UB-BPF, respectively.

B. Cross-Sectional Effect of Integrated Dual-Band BPF and MS With Sample Load

The independence of a hybrid device is crucial to ensure its unambiguous operation. Here, the cross-sectional effect of the integrated dual-band BPF and MS was evaluated by varying the loaded sample. **Fig. 11(a)** shows a measurement result of $|S_{21}|$ with broadband response of the dual band BPF and MS for different SUT solid material. Here, we utilized samples with permittivity and dielectric loss characteristics as follows, RO5880 ($\varepsilon_r = 2.2$, tan $\delta = 0.0009$), RO4003C ($\varepsilon_r = 3.55$, tan $\delta = 0.0027$), FR4 ($\varepsilon_r = 4.3$, tan $\delta = 0.0265$), RO3006 ($\varepsilon_r = 6.15$, tan $\delta = 0.0025$), and TM 10 ($\varepsilon_r = 9.5$, tan $\delta = 0.0022$). The ambient temperature during the measurements was maintained at 25°C. The measurement results show that with the increase of ε_r of the sample, the frequency value of the peak MS will shift to the left or have a lower frequency. In this study, TM10 represented the highest ε_r value, while air represented the lowest ε_r value. In other words, the initial condition of the device is still without a sample.

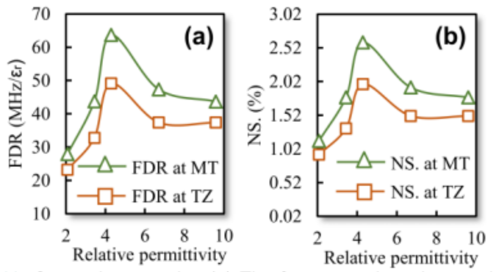

Fig. 14. Comparison results. (a) The frequency detection resolution (FDR) value, (b) normalized sensitivity (NS) at the maximum transmission (MT) and transmission zeros (TZ).

Fig. 11(b) depicts the measurement results of $|S_{11}|$ for the dual-band BPF and MS with different SUT solid materials. The $|S11|$ value is lower than -10 dB for the dual-band BPF, and vice versa for the MS. Moreover, there are several interesting observations regarding the cross-sectional effect of the dual-band BPF and MS.

1) After MS is loaded with a sample, the dual-band BPF maintains a constant value of $|S_{21}|$ and $|S_{11}|$.
2) The bandwidth of the dual-band BPF, both LB-BPF and UB-BPF, remains fixed and stable.
3) The MS has $|S_{21}| < -3$ dB and $|S_{11}| > -10$ dB, which means it will not function as a BPF and will reduce ambiguity.

Overall, the dual-band BPF exhibits stable and independent characteristics and is not influenced by the MS. Additionally, it should be noted that the proposed device has independent capability. This means that each parameter works standalone without interfering with each other. Moreover, the reflection phase is also another microwave sensor technique. However, it has several disadvantages, such as more complicated measurements and a limited dynamic range with ambiguous values if it rotates more than 180 degrees.

C. Sensor Evaluation and Comparison Result

In detail, **Fig. 12(a).** shows a measurement result of $|S_{21}|$ with detail around the MT and TZ value for MS evaluation. We can observe the shifting of MT and TZ after the MS is loaded with different samples. Then, we recorded the frequency values of MT and TZ and plotted them as shown in **Fig 12(b)**. It should be noted that the measurement of the MS was conducted three times for repeatability. The variation in the results of MT and TZ is low, indicating data stability. In detail, it also depicts the relationship between the permittivity of the sample and the frequency of MT and TZ. It is shown that higher sample permittivity leads to lower frequency for both MT and TZ. The next step is to calculate the relationship between $\Delta\varepsilon_r$ and Δf, as shown in **Fig 13(a).** This data is crucial for calculating the frequency detection resolution (FDR) value and normalized sensitivity (NS). Here, the Δf and $\Delta\varepsilon_r$ are compared to the unloaded condition (such as f_{air} and $\varepsilon_r = 1.00$) with three times repeatability.

Moreover, **Fig. 13(b)** depicts the relationship between the frequency values of MT and TZ and the ε_r values for regression purposes. Therefore, the ε_r values can be extracted from frequency. The ε_r values are calculated by:

$$\begin{pmatrix}\varepsilon_{r(MT)}\\ \varepsilon_{r(TZ)}\end{pmatrix} = \begin{pmatrix}19.669 & -116.90\\ 27.510 & 146.11\end{pmatrix}\begin{pmatrix}f^2\\ f\end{pmatrix} + \begin{pmatrix}170.23\\ 194.25\end{pmatrix} \qquad (7)$$

where f is frequency of MT or TZ. Then, the $\varepsilon_{r(\mathrm{MT})}$ or $\varepsilon_{r(\mathrm{TZ})}$ are relative permittivity values using MT or TZ, respectively.

Figs. 14 (a)-(b) show the comparison result of FDR and NS using MT or TZ-based methods. The equations for FDR and NS can be found in [25]–[27] for FDR and [28]–[30] for NS. In detail, **Fig. 14 (a)** depicts the maximum FDR values as 63.70 MHz/ε_r and 49.11 MHz/ε_r for MT and TZ-based, respectively. Moreover, **Fig. 14 (b)** depicts the comparison results of NS using MT or TZ-based methods. The maximum NS values are 2.60 % and 1.98 % for MT and TZ-based methods, respectively. The MT has a slightly higher FDR and NS compared to TZ-based sensors. This occurs because the E-field values of MT are higher than those of TZ. However, TZ can serve as an alternative sensor when the MT does not function as intended.

Table 1 presents a comprehensive comparison of the integrated MS-based sensor with other devices, including the state of the art. The proposed device exhibits several unique parameters and integrated features: 1) The dual-band BPFs offer controllable frequency center and bandwidth. 2) The proposed device does not require additional insulators or power supplies, making it simple and suitable for wireless communication and IoT applications where power supply is limited. 3) The responses of the dual-band BPF and MS are unambiguous and distinctive, with clear interpretations. They exhibit independent performances and do not influence each other. 4) The utilization of the MT and TZ approach provides a higher degree of freedom, especially for material characterization, while also facilitating more robust analysis. Then, 5) the hybrid device combines simultaneous functionalities and significantly reduces the number of ports by 66% (from 6 ports to 2 ports) with a simple single-layered substrate design, ensuring ease of implementation.

V. CONCLUSION

A multifunctional, integrated, and highly independent dual-band BPF with MS for RF communication and solid material characterization was successfully developed. The proposed device unifies MUX-DEMUX. As a result, the dual-band BPF has frequency centers of 1.80 GHz (LB-BPF) and 2.56 GHz (UB-BPF) suitable for 4G and 5G applications, respectively. Moreover, the dual-band BPF exhibits independent characteristics, with easily controllable center frequencies and fractional bandwidths. The MS achieved a normalized sensitivity of 2.60% and 1.98% for MT and TZ, respectively. Interestingly, the integration of LB-BPF, UB-BPF, and MS shows independent performances and does not influence each other. Finally, compared to prior structures, the proposed design offers several advantages including a simple structure based on a 2-port single-layered substrate design.

ACKNOWLEDGMENT

Muh. Wildan is with Politeknik Penerbangan Indonesia Curug, Jl. Raya PLP Curug, Indonesia.

Dwi Astuti Cahyasiwi is with Departement of Electrical Engineering, Universitas Muhammadiyah Prof. Dr Hamka, Jakarta, Indonesia.

Yusnita Rahayu is with Departement of Electrical Engineering, Universitas Riau, Pekanbaru, Indonesia.

Hepi Ludiyati is with Bandung State of Polytechnic, Indonesia.

Ken Paramayudha and Yuyu Wahyu are with Research Center for Telecommunication, National Research and Innovation Agency (BRIN), Bandung, Indonesia.

Syah Alam is with Department of Electrical Engineering, Universitas Trisakti, Grogol, Jakarta, 11440, Indonesia.

Mudrik Alaydrus are with Department of Electrical Engineering, Universitas Mercu Buana, Jakarta, 11650, Indonesia.

Jun Kondoh is with Graduate School of Science and Technology, Shizuoka University, 3-5-1 Johoku, Naka-ku, Hamamatsu-shi 432-8561, Japan.

REFERENCES

[1] A. Ebrahimi *et al.*, "Highly Sensitive Phase-Variation Dielectric Constant Sensor Based on a Capacitively-Loaded Slow-Wave Transmission Line," *IEEE Trans. Circuits Syst. I Regul. Pap.*, vol. 68, no. 7, pp. 2787–2799, 2021, doi: 10.1109/TCSI.2021.3074570.

[2] P. Casacuberta, P. Velez, J. Munoz-Enano, L. Su, and F. Martin, "Highly Sensitive Reflective-Mode Phase-Variation Permittivity Sensors Using Coupled Line Sections," *IEEE Trans. Microw. Theory Tech.*, pp. 1–15, 2023, doi: 10.1109/tmtt.2023.3234272.

[3] M. Baghelani and O. Hasan-Nejad, "Highly Sensitive Microwave Sensor for High Precision Sensing of Water Contamination in Mineral Oil," *IEEE Sens. J.*, vol. 21, no. 12, pp. 13247–13254, 2021, doi: 10.1109/JSEN.2021.3071839.

[4] A. Ghaderi, A. Golestanifar, and F. Shama, "Design of a compact microstrip tunable dual-band bandpass filter," *AEU - Int. J. Electron. Commun.*, vol. 82, no. October, pp. 391–396, 2017, doi: 10.1016/j.aeue.2017.10.002.

[5] F. Wei, L. Chen, and X. W. Shi, "Compact dual-mode dual-band bandpass filter with wide stopband," *J. Electromagn. Waves Appl.*, vol. 26, no. 11–12, pp. 1441–1447, 2012, doi: 10.1080/09205071.2012.701575.

[6] F. Wei, C. Y. Zhang, C. Zeng, and X. W. Shi, "A Reconfigurable Balanced Dual-Band Bandpass Filter with Constant Absolute Bandwidth and High Selectivity," *IEEE Trans. Microw. Theory Tech.*, vol. 69, no. 9, pp. 4029–4040, 2021, doi: 10.1109/TMTT.2021.3093907.

[7] H. Saghlatoon, R. Mirzavand, and P. Mousavi, "Fixed-Frequency Low-Loss Dielectric Material Sensing Transmitter," *IEEE Trans. Ind. Electron.*, vol. 68, no. 4, pp. 3517–3526, 2021.

[8] M. Adhikary, A. Biswas, and M. J. Akhtar, "Active Integrated Antenna Based Permittivity Sensing Tag," *IEEE Sensors Lett.*, vol. 1, no. 6, 2017, doi: 10.1109/LSENS.2017.2768560.

[9] D. D. Dinh and M. J. Lancaster, "Microwave power sensors with integrated filtering function for transfer power standards," *IEEE Microw. Wirel. Components Lett.*, vol. 30, no. 3, pp. 308–311, 2020, doi: 10.1109/LMWC.2020.2969570.

[10] Z. Shaterian and M. Mrozowski, "A Multifunctional Microwave Filter/Sensor Component Using a Split Ring Resonator Loaded Transmission Line," *IEEE Microw. Wirel. Components Lett.*, pp. 3–6,

2022, doi: 10.1109/LMWC.2022.3208373.

[11] R. Mirzavand, M. M. Honari, and P. Mousavi, "High-Resolution Balanced Microwave Material Sensor with Extended Dielectric Range," *IEEE Trans. Ind. Electron*., vol. 64, no. 2, pp. 1552–1560, 2017, doi: 10.1109/TIE.2016.2612621.

[12] S. Alam, Z. Zakaria, I. Surjati, N. Azwan, and M. Alaydrus, "Multifunctional of dual-band permittivity sensors with antenna using multicascode T-shaped resonators for simultaneous measurement of solid materials and data transfer capabilities," *Measurement*, vol. 217, no. April, p. 113078, 2023, doi: 10.1016/j.measurement.2023.113078.

[13] J. Cui, A. Zhang, and S. Yan, "Microfluidic Filtering Antenna for Sensor Application," *2020 13th UK-Europe-China Work. Millimetre-Waves Terahertz Technol. UCMMT 2020 - Proc*., pp. 8–9, 2020, doi: 10.1109/UCMMT49983.2020.9296074.

[14] C. H. Chio, K. W. Tam, and R. Gomez-Garcia, "Filtering Angular Displacement Sensor Based on Transversal Section with Parallel-Coupled-Line Path and U-Shaped Coupled Slotline," *IEEE Sens. J*., vol. 22, no. 2, pp. 1218–1226, 2022, doi: 10.1109/JSEN.2021.3133452.

[15] H. Saghlatoon, M. M. Honari, R. Mirzavand, and P. Mousavi, "Substrate integrated waveguide groove sensor antenna for permittivity measurements," *IET Conf. Publ.*, vol. 2018, no. CP741, pp. 4–6, 2018, doi: 10.1049/cp.2018.0648.

[16] J. Lu, L. Ma, C. Gu, and J. Mao, "A High-Isolation Duplexer With Mismatched Load Impedance for Integrated Sensing and Communication," *IEEE Microw. Wirel. Components Lett*., vol. 32, no. 9, pp. 1127–1130, 2022, doi: 10.1109/LMWC.2022.3166259.

[17] H. Saghlatoon, R. Mirzavand, M. M. Honari, and P. Mousavi, "Sensor Antenna Transmitter System for Material Detection in Wireless-Sensor-Node Applications," *IEEE Sens. J.*, vol. 18, no. 21, pp. 8812–8819, 2018, doi: 10.1109/JSEN.2018.2868006.

[18] M. Behdani, M. M. H. Kalateh, H. Saghlatoon, J. Melzer, and R. Mirzavand, "High-Resolution Dielectric Constant Measurement Using a Sensor Antenna with an Allocated Link for Data Transmission," *IEEE Sens. J.*, vol. 20, no. 24, pp. 14827–14835, 2020, doi: 10.1109/JSEN.2020.3012055.

[19] R. Mirzavand, M. M. Honari, and P. Mousavi, "High-resolution dielectric sensor based on injection-locked oscillators," *IEEE Sens. J.*, vol. 18, no. 1, pp. 141–148, 2018, doi: 10.1109/JSEN.2017.2772923.

[20] Z. Shaterian and M. Mrozowski, "Multifunctional Bandpass Filter/Displacement Sensor Component," *IEEE Access*, vol. 11, no. February, pp. 1–1, 2023, doi: 10.1109/access.2023.3258545.

[21] T. Alam and M. Cheffena, "Integrated Microwave Antenna/Sensor for Sensing and Communication Applications," *IEEE Trans. Microw. Theory Tech*., vol. 70, no. 11, pp. 5289–5300, 2022, doi: 10.1109/TMTT.2022.3199242.

[22] C. H. Chio, R. Gomez-Garcia, L. Yang, K. W. Tam, W. W. Choi, and S. K. Ho, "An Angular-Displacement Microwave Sensor Using an Unequal-Length-Bi-Path Transversal Filtering Section," *IEEE Sens. J.*, vol. 20, no. 2, pp. 715–722, 2020, doi: 10.1109/JSEN.2019.2943640.

[23] O. N. Microwave, "Coupled Strip Transmission Line and Directional Couplers," *IRE Trans. Circuit Theory*, no. 5, pp. 75–81, 1956.

[24] H. R. Ahn, *Asymmetric Passive Components in Microwave Integrated Circuits.* A John Wiley & Sons, Inc., 2005.

[25] S. Kiani, P. Rezaei, and M. Navaei, "Dual-sensing and dual-frequency microwave SRR sensor for liquid samples permittivity detection," *Meas. J. Int. Meas. Confed*., vol. 160, p. 107805, 2020, doi: 10.1016/j.measurement.2020.107805.

[26] S. Kiani, P. Rezaei, and M. Fakhr, "Dual-Frequency Microwave Resonant Sensor to Detect Noninvasive Glucose-Level Changes through the Fingertip," *IEEE Trans. Instrum. Meas.*, vol. 70, 2021, doi: 10.1109/TIM.2021.3052011.

[27] S. Kiani, P. Rezaei, M. Navaei, and M. S. Abrishamian, "Microwave Sensor for Detection of Solid Material Permittivity in Single/Multilayer Samples With High Quality Factor," *IEEE Sens. J.*, vol. 18, no. 24, pp. 9971–9977, 2018, doi: 10.1109/JSEN.2018.2873544.

[28] A. Ebrahimi, J. Scott, and K. Ghorbani, "Ultrahigh-Sensitivity Microwave Sensor for Microfluidic Complex Permittivity Measurement," *IEEE Trans. Microw. Theory Tech.*, vol. 67, no. 10, pp. 4269–4277, 2019, doi: 10.1109/TMTT.2019.2932737.

[29] A. Ebrahimi, W. Withayachumnankul, S. Al-Sarawi, and D. Abbott, "High-Sensitivity Metamaterial-Inspired Sensor for Microfluidic Dielectric Characterization," vol. 14, no. 5, pp. 1345–1351, 2014.

[30] A. Ebrahimi, F. J. Tovar-Lopez, J. Scott, and K. Ghorbani, "Differential microwave sensor for characterization of glycerol–water solutions," *Sensors Actuators, B Chem.*, vol. 321, no. July, p. 128561, 2020, doi: 10.1016/j.snb.2020.128561.

[31] M. Adhikary, A. Biswas, and M. J. Akhtar, "Active Integrated Antenna Based Permittivity Sensing Tag," *IEEE Sensors Lett.*, vol. 1, no. 6, pp. 1–4, 2017, doi: 10.1109/LSENS.2017.2768560.

[32] A. Ebrahimi, J. Scott, and K. Ghorbani, "Transmission lines terminated with LC resonators for differential permittivity sensing," *IEEE Microw. Wirel. Components Lett.*, vol. 28, no. 12, pp. 1149–1151, 2018, doi: 10.1109/LMWC.2018.2875996.

[33] S. Alam, Z. Zakaria, I. Surjati, N. A. Shairi, M. Alaydrus, and T. Firmansyah, "Dual-Band Independent Permittivity Sensor Using Single-Port with a Pair of U-Shaped Structures for Solid Material Detection," *IEEE Sens. J.*, vol. 22, no. 16, pp. 16111–16119, 2022, doi: 10.1109/JSEN.2022.3191345.

Dwi Astuti Cahyasiwi - Integrated and Independent Solid Microwave Sensor with Dual-Band Bandpass Filter Through Unified Mux-Demux Structure

ORIGINALITY REPORT

13%	9%	11%	4%
SIMILARITY INDEX	INTERNET SOURCES	PUBLICATIONS	STUDENT PAPERS

PRIMARY SOURCES

1	www.researchgate.net Internet Source	3%
2	Teguh Firmansyah, Supriyanto Praptodiyono, Imamul Muttakin, Ken Paramayudha et al. "Multifunctional Glass Microfluidic Microwave Sensor Attenuator for Detection of Permittivity and Conductivity With Device Protection", IEEE Sensors Journal, 2024 Publication	2%
3	www.karyailmiah.trisakti.ac.id Internet Source	1%
4	www.mdpi.com Internet Source	1%
5	eprints.untirta.ac.id Internet Source	<1%
6	Joong Han Yoon, Sang Jin Oh, Woo Su Kim. "Design of microstrip-fed monopole antenna with two branch strips and a rectangular slit	<1%

	ground for dual-band WLAN operations", Microwave and Optical Technology Letters, 2011 Publication	
7	www.radioeng.cz Internet Source	<1 %
8	tentzeris.ece.gatech.edu Internet Source	<1 %
9	Alqaisy, Mushtaq A., C. Chakrabraty, J. Ali, A. R. H. Alhawari, and Tale Saeidi. "Reconfigurable Bandwidth and Tunable Dual-Band Bandpass Filter Design for Ultra-Wideband (UWB) Applications", Electromagnetics, 2016. Publication	<1 %
10	ddd.uab.cat Internet Source	<1 %
11	Pal, Manimala, Biswajit Sarkar, Pankaj Sarkar, and Rowdra Ghatak. "A dual-band bandpass filter using integrated stepped impedance resonators", International Journal of Electronics Letters, 2014. Publication	<1 %
12	Daotong Li, Ju-An Wang, Ying Liu, Zhen Chen. "Miniaturized Dual-Band Bandpass Filter With Sharp Roll-Off Using Ring-Loaded Resonator", IEEE Access, 2020 Publication	<1 %

13	Wenjie Feng, Wenquan Che. "Novel Ultra-Wideband Bandpass Filter Using Shorted Coupled Lines and Transversal Transmission Line", IEEE Microwave and Wireless Components Letters, 2010 Publication	<1%
14	Y. Li, C. Wang, N.Y. Kim. "A compact dual-band bandpass filter with high design flexibility using fully isolated coupling paths", Microwave and Optical Technology Letters, 2014 Publication	<1%
15	pdfs.semanticscholar.org Internet Source	<1%
16	scholar.unair.ac.id Internet Source	<1%
17	vis.pku.edu.cn Internet Source	<1%
18	Hamidreza Laribi, Kambiz Moez, Hossein Rouhani, Rashid Mirzavand. "Temperature Compensated Dielectric Constant Sensor Using Dual-Mode Triangular Structure", IEEE Sensors Journal, 2023 Publication	<1%
19	Submitted to Yakın Doğu Üniversitesi Student Paper	<1%

20	doaj.org Internet Source	<1%
21	Zahra Mehrjoo, Amir Ebrahimi, Kamran Ghorbani. "Microwave Resonance-Based Reflective Mode Displacement Sensor With Wide Dynamic Range", IEEE Transactions on Instrumentation and Measurement, 2022 Publication	<1%
22	cimitec.uab.cat Internet Source	<1%
23	eureka.patsnap.com Internet Source	<1%
24	J. G. Domingos de Oliveira, S. B. Paiva, J. G. Duarte Junior, L. F. V. Torres Costa, V. P. Silva Neto, A. G. D'Assuncao. "Bio-inspired Sensor for the Electrical Permittivity Characterization of Dielectric Materials", 2020 14th European Conference on Antennas and Propagation (EuCAP), 2020 Publication	<1%
25	Li, Daotong, Yonghong Zhang, Kaijun Song, Kaida Xu, and Joshua L.-W. Li. "Miniaturized Close Dual-Band Bandpass Filter Based on Short Stub-Loaded Stepped-Impedance Resonators", Electromagnetics, 2015. Publication	<1%

26	Teguh Firmansyah, Supriyanto Praptodinoyo, Romi Wiryadinata, Suhendar Suhendar et al. "Dual-wideband band pass filter using folded cross-stub stepped impedance resonator", Microwave and Optical Technology Letters, 2017 Publication	<1 %
27	Xiaowu Zhan, Zong-Xi Tang, Hanli Liu, Yunqiu Wu, Biao Zhang. "COMPACT MULTIBAND TRANSVERSAL BANDPASS FILTERS WITH MULTIPLE TRANSMISSION ZEROES", Progress In Electromagnetics Research Letters, 2012 Publication	<1 %
28	jees.kr Internet Source	<1 %
29	www.eng.shizuoka.ac.jp Internet Source	<1 %
30	Alok Kumar, Cong Wang, Fan-Yi Meng, Cheng-Peng Jiang, Guo-Feng Yan, Meng Zhao, Chang-Qiang Jing, Lei Wang. "Ultrafast Detection and Discrimination of Methanol Gas Using a Polyindole-Embedded Substrate Integrated Waveguide Microwave Sensor", ACS Sensors, 2020 Publication	<1 %
31	Antonious Rajagukguk, Ciptian Weried Priananda, Dedet Candra Riawan, Soedibyo,	<1 %

	Mochamad Ashari. "Novel derivative cluster area methods (DCAM) for power optimization of PV farm under dinamically shading effect", 2017 15th International Conference on Quality in Research (QiR) : International Symposium on Electrical and Computer Engineering, 2017 Publication	
32	Hang Chen, Jin-Xu Xu, Wenhua Chen, Xiu Yin Zhang. "High-Efficiency Dual-Band Filtering Doherty Power Amplifier Based on Multi-Function Circuit", IEEE Transactions on Microwave Theory and Techniques, 2022 Publication	<1 %
33	Li, Zhi-Hui, and Qing-Xin Chu. "Compact dual-band bandpass filter using a novel dual-mode resonator", 2012 International Conference on Microwave and Millimeter Wave Technology (ICMMT), 2012. Publication	<1 %
34	Qing-Xin Chu. "A compact dual-band filter using S-shaped stepped impedance resonators", 2008 International Conference on Microwave and Millimeter Wave Technology, 04/2008 Publication	<1 %
35	Shuren Jiang, Guohua Liu, Mingyang Wang, Yuezhi Wu, Jianwei Zhou. "Design of High-	<1 %

	Sensitivity Microfluidic Sensor Based on CSRR With Interdigital Structure", IEEE Sensors Journal, 2023 Publication	
36	Wei, Feng, Qiu Lin Huang, Wen-Tao Li, and Xiao-Wei Shi. "A compact quad-band band-pass filter using novel stub-loaded SIR structure", Microwave and Optical Technology Letters, 2014. Publication	<1%
37	Zaynab Attoun, Nader Shafi, Youssef Tawk, Joseph Costantine, Elie Shammas. "Wearable Flexible Radio Frequency Filtering System for Muscle Contraction Monitoring", IEEE Journal of Microwaves, 2024 Publication	<1%
38	abcelectronique.com Internet Source	<1%
39	ejournal.upm.ac.id Internet Source	<1%
40	era.library.ualberta.ca Internet Source	<1%
41	mostwiedzy.pl Internet Source	<1%
42	scholarcommons.sc.edu Internet Source	<1%

43	worldwidescience.org Internet Source	<1%
44	www.scielo.br Internet Source	<1%
45	He, Zetao, Yu Shi, and Xubo Wei. "Compact dual-band BPF with improved stopband", 2014 15th International Conference on Electronic Packaging Technology, 2014. Publication	<1%
46	Min-Hang Weng. "Compact dual-band bandpass filter with enhanced feed coupling structures", Microwave and Optical Technology Letters, 01/2007 Publication	<1%
47	Saeed Javadizadeh, Majid Badieirostami, Mahmoud Shahabadi. "Ultrasensitive miniaturized planar microwave sensor for characterization of water–alcohol mixtures", Scientific Reports, 2023 Publication	<1%
48	Syah Alam, Zahriladha Zakaria, Indra Surjati, Noor Azwan Shairi, Mudrik Alaydrus, Teguh Firmansyah. "Multifunctional of Dual-Band Permittivity Sensors with Antenna using Multicascode T-shaped Resonators for Simultaneous Measurement of Solid Materials	<1%

	and Data Transfer Capabilities", Measurement, 2023 Publication	
49	Y.-K. SU. "Design of Dual-Band Bandpass Filter with Quasi-Elliptic Function Response for WLANs", IEICE Transactions on Electronics, 01/01/2007 Publication	<1%
50	Springer Theses, 2016. Publication	<1%

Exclude quotes	Off	Exclude matches	Off
Exclude bibliography	On		